Two Types of Negative Capacitance of $BaTiO_3/SnO_2$:F Heterojunction: Origins and Ultraviolet Modulation

Jiayi He(何佳祎)*[1], Lin Liu(刘琳)*[2], Zeyu Xiao(肖泽宇)*[1], Xiaomei Lu(吕笑梅)[1,3,a)], Xueli Hu(胡雪莉)[1], Fengzhen Huang(黄凤珍)[1,3,b)], Shuyu Xiao(肖疏雨)[4,c)], Yingsong Xia(夏银松)[1], Jielin Zha(查节林)[1], Jiayi Chen(陈嘉怡)[1], Jinsong Zhu(朱劲松)[1,3]

* These authors contributed equally to this work.

[1] National Laboratory of Solid State Microstructures and Physics School, Nanjing University, Nanjing 210093, People's Republic of China

[2] Engineering College, Lishui University, Lishui 323000, People's Republic of China

[3] Collaborative Innovation Center of Advanced Microstructures, Nanjing 210093, People's Republic of China

[4] School of Biomedical Engineering and Informatics, Nanjing Medical University, Nanjing 211166, People's Republic of China

[a, b, c)]Corresponding Author:

[a)]E-mail: xiaomeil@nju.edu.cn

[b)]E-mail: fzhuang@nju.edu.cn

[c)]E-mail: syxiao@njmu.edu.cn+

Abstract: The negative capacitance effect in ferroelectric materials holds significant potential for reducing the energy consumption of transistors, and the experimental demonstration and mechanism analysis of these phenomena have attracted substantial attention. In this study, by depositing ferroelectric $BaTiO_3$ thin films with thicknesses

ranging from 212 to 390 nm onto semiconducting SnO_2:F substrates, we directly measured two distinct types of negative capacitance. One type, observed under large bias (NCl), originates primarily from injection and delayed migration of carriers across the ferroelectric/semiconductor interface, while the other type, captured under small bias for the 390 nm sample with a larger initial polarization, corresponds to the intermediate state of ferroelectric polarization switching where intrinsic negative capacitance emerges (NCs). The direct measurement of the latter was enabled by a "dual-delay" mechanism established by the stepwise DC bias and oxygen vacancy migration, which effectively delayed both the ferroelectric polarization switching and the charge compensation, thereby provided a critical window for capturing the transient process of polarization switching. For the 390 nm $BaTiO_3$ film, the total capacitance measured at biases of 16 V and −16 V were approximately −50.69 nF and −7.92 nF (100 Hz), respectively. Furthermore, it was found that 275 nm ultraviolet illumination could modulate the negative capacitance by altering carrier transport and charge-screening behavior, resulting in the magnitude changes of the negative capacitance under large bias and the disappearance of negative capacitance under small bias. These findings contribute to a deeper understanding of the physical mechanisms underlying negative capacitance and provide valuable insights for the development of novel low-power integrated electronic devices based on ferroelectric materials.

Key Words: $BaTiO_3$, Ferroelectric/semiconductor heterojunction, Negative capacitance, Light modulation

PACS: 77.80.Fm, 77.55.fe, 73.40.Lq, 73.50.Pz, 77.22.Gm

1. Introduction

Negative capacitance (NC) in ferroelectrics, predicted by Landau-Ginzburg-Devonshire theory through the negative slope of polarization-electric field ($P-E$) curves near the origin, [1-4] has garnered significant attention in recent years.[5-8] Zhao *et al.* demonstrated a 2D ferroelectric $CuInP_2S_6$(CIPS)-based ferroelectric negative capacitance field-effect transistor (FE-NCFET) with a *SS* of 14 mV/dec at 0.3 V using WS_2 and Al_2O_3 passivation layer.[9] Kamaei *et al.* achieved an average *SS* of 50 mV/dec in FE-NCFETs with Si-doped HfO_2 gate stacks integrated with WSe_2.[10] Chi *et al.* reduced the minimum *SS* to 15.2 mV/dec in CIPS/MoS_2 heterostructures by applying magnetostrictive strain from a Terfenol-D substrate.[11] While these studies demonstrate the potential of the NC effect for low-power electronics, the underlying phenomena and related mechanisms remain insufficiently explored.

Intrinsic NC of ferroelectrics occurs during dynamic polarization switching, making its detection and analysis challenging.[12-16] Typically, NC is displayed indirectly by two experimental methods: steady state and transient state.[17-20] Steady NC refers to a stable state in a ferroelectric-dielectric series circuit under certain conditions, where the total capacitance exceeds the dielectric layer capacitance. For example, Tasneem *et al.* connected ferroelectric $Hf_{0.5}Zr_{0.5}O_2$ with amorphous HfO_2 in series.[20] Qiao *et al.* fabricated $Hf_{0.5}Zr_{0.5}O_2$-Al_2O_3 series capacitors.[21] It has been reported that once the series dielectric layer exceeds a certain thickness, the ferroelectric layer can no longer acquire sufficient screening charges, leading to the suppression of polarization switching and the eventual emergence of steady-state negative capacitance.[22,23] Transient negative capacitance refers to the case where a ferroelectric material is connected in series with a fixed resistor. The screening

charges from the external circuit cannot keep up with the change of polarization charges during switching. By subtracting the resistive voltage drop, one can capture a short transient regime where the actual voltage across the ferroelectric layer and the charge amount vary inversely with time, as was done on PZT,[1] CIPS,[24] and V:HfO_2.[15] By constructing a (111)-PZT ferroelectric superdomain, Chen *et al.* even detected multilevel transient negative capacitance.[16]

Direct detection of negative capacitance has also been reported in the literatures. In 2016, Hou *et al.* observed negative capacitance in $BaTiO_3$/$BiFeO_3$ bilayer capacitors, with values of several nanofarads at bias >3.5 V and frequencies $<10^4$ Hz.[25] In 2020, Wang *et al.* measured negative capacitance in the nanofarad range for $BaTiO_3$/$SrTiO_3$ core-shell particles under MHz-level electric fields.[26] Acharya *et al.* detected negative capacitance in FeO_x/Al_2O_3 capacitors, with values of 0.015 F/m^2 at ±10 mV bias and 5 kHz frequency.[27] In 2023, we discovered negative capacitance in $BaTiO_3$/p-Si heterojunctions, with values of 0.1 μF/cm^2 at -4 V bias and 10^2 Hz frequency.[28] It should be noted that, previously-reported directly measured negative capacitance relied mostly on the interfacial charge distribution/migration modified by applying external stress or by changing the amplitude and frequency of applied voltage. They can hardly be mechanically correlated with the intermediate polarization switching state where intrinsic ferroelectric negative capacitance emerges.

In this work, $BaTiO_3$ (BTO) films were prepared on n-type SnO_2:F (FTO) substrates to construct ferroelectric/semiconductor heterojunctions. BTO, as a widely used classic ferroelectrics,[29-31] possesses simple perovskite structure, large

spontaneous polarization, and reproducible domain switching. While FTO, as a commonly used oxide electrode in solar cells,[32,33] not only provides a semiconductor interface (rather than a metallic one), but also favors optical gating due to its high transparency. For this BTO/FTO heterostructure, we present interesting experimental results where two negative capacitance regions were directly measured at low frequencies: one, similar to our previous findings in $BaTiO_3$/p-Si heterostructures, is the extrinsic negative capacitance region under large bias (NCl) corresponding to carrier injection and lagged migration across the interface.[28,34] The other, more importantly, marks the first observation of the negative capacitance region under small bias (NCs), corresponding to the intermediate state of polarization switching. The successful measurement of the latter is enabled by a "dual-delay" mechanism: stepwise DC bias retards polarization switching, while the relaxation migration of easily interface-trapped oxygen vacancies delays shielding charge compensation, providing a critical time window to capture the polarization reversal dynamics. In addition, current approaches to modulating negative capacitance rely mainly on electrical means. In this work, 275 nm ultraviolet illumination was introduced, and the generation and transport of photocarriers were utilized to achieve noninvasive modulation of the negative capacitance. This work provides valuable insights for revealing the mechanism and promoting the applications of negative capacitance.

2. Experimental Methods

$BaTiO_3$(BTO) films were deposited on n-type SnO_2:F (FTO, sheet resistance: 15 Ω) substrates by pulsed laser deposition (λ=248 nm) at a substrate temperature of 650 °C, an oxygen pressure of 20 Pa, a fixed target-to-substrate distance of 50 mm, a laser energy of 250 mJ, and a repetition frequency of 5 Hz. BTO films with different

thicknesses (212, 302, and 390 nm) were obtained by controlling the deposition time (27, 44, and 60 min). Before the electrical measurement, circular Pt electrodes with 2 mm diameter and 20 nm thickness were deposited on top of the film by magnetron sputtering. The microstructure of the films was characterized by X-ray diffraction (XRD, Bruker D8 Advance, Cu Kα), scanning electron microscopy (SEM, ZEISS Gemini 500) and atomic force microscopy (AFM, Bruker icon). The absorption spectra of the samples were measured by ultraviolet-visible spectrophotometer (Shimadzu, UV-3600), and the binding states of O1s electrons and Ti 2p electrons were analyzed by X-ray photoelectron spectroscopy (XPS, ESCALab MK-II). A standard ferroelectric tester (TF-2000, aix-ACCT, Aachen, Germany), a source measure unit (Keithley 6482), and an LCR impedance analyzer (4294A, Agilent, Santa Clara, CA) were used to measure the polarization-voltage (*P-V*) hysteresis loops, current-voltage (*I-V*) curves, and capacitance-voltage/frequency (*C-V/f*) curves, respectively. The power density of the 275 nm ultraviolet light was about 5600 $\mu W/cm^2$, calibrated by an ultraviolet radiometer (LS125).

3. Results and Discussion

3.1 Basic Structural characteristics and Electrical Properties

The cross-sectional SEM images and corresponding EDS elemental analysis of the BTO films with three different thicknesses (212 nm, 302 nm, and 390 nm) prepared with increasing deposition time are shown in Figure S1. The BTO films continuously cover the surface of the FTO substrates with tight adhesion and clear layering, exhibiting uniform thickness and no obvious structural defects. The signals of Ba/Ti and Sn concentrate in the BTO and FTO regions, respectively, indicating no

interdiffusion between these two materials and confirming the formation of a high-quality heterointerface. The film surfaces are smooth and dense, with an average grain size (AGS) ranging from approximately 0.18 to 0.27 μm and a root-mean-square (RMS) roughness varying between 12.0 and 14.8 nm [Figure 1(a–c)]. The X-ray diffraction (XRD) patterns indicate a polycrystalline tetragonal phase [Figure 1(d)], with the (110) diffraction peak significantly higher than the other peaks (PDF#05-0626).

Figure 1(e-g) present the O 1s XPS spectra of the BTO films. Each spectrum can be fitted with two sub-peaks: O1 at ~529.6 eV, corresponding to lattice oxygen, and O2 at ~531.2 eV, associated with adsorbed oxygen (indicating the relative content of oxygen vacancies). As the film thickness increases, the ratio of the integral intensities of O2 to O1 (I_{O2}/I_{O1}) decreases, with values of 1.07, 0.95, and 0.85 for the 212 nm, 302 nm, and 390 nm thickness, respectively, revealing a gradual reduction in oxygen vacancies, and consistent with the increased relative content of Ti^{4+} compared to Ti^{3+} ions (Figure S2).[35,36]

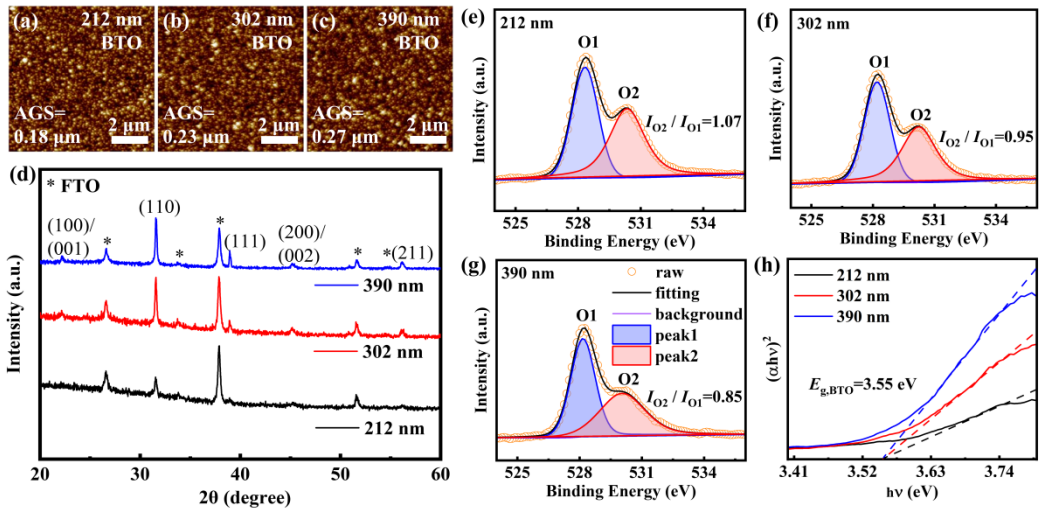


Figure 1. (a-c) AFM surface morphology. (d) XRD patterns of the $BaTiO_3$ films with

different thicknesses. (e-g) O 1s XPS peak fitting. (h) Tauc plots of BTO films with different thicknesses, the bandgap fitted by the Tauc plot: $(\alpha hv)^2 = b(hv - E_g)$, where is α the absorption coefficient, h is Planck's constant, v is the incident photon frequency, b is a constant, E_g is the bandgap.

Figure 1h is the Tauc plots of the optical absorption. The bandgaps (E_g) of the three BTO films with different thicknesses are nearly identical, being about 3.55 eV. The valence-band (VB) spectra (Figure S3) show that $E_{\mathrm{VBM}}^{E_f}$, namely the energy difference between the Fermi level E_f and the valence-band maximum E_{VBM}, gradually decreases from 2.15 eV to 2.07 eV and finally to 2.01 eV for the BTO films with thicknesses of 212, 302, and 390 nm, respectively. These values are all larger than half of the BTO band gap (E_g = 3.55 eV), indicating weak n-type conductivity of the films. Since oxygen vacancies carry positive charges, it is generally accepted that the charge carriers in samples with oxygen vacancies are negatively charged electrons. As the film thickness increases, the decrease in $E_{\mathrm{VBM}}^{E_f}$ implies the lowering of E_f while the increasing of E_c-E_f (E_c, conduction band minimum), which means, the electron carrier concentration n ($\propto \exp[-(E_c-E_f)/kT]$) reduces, consistent with the aforementioned decrease of oxygen vacancies.

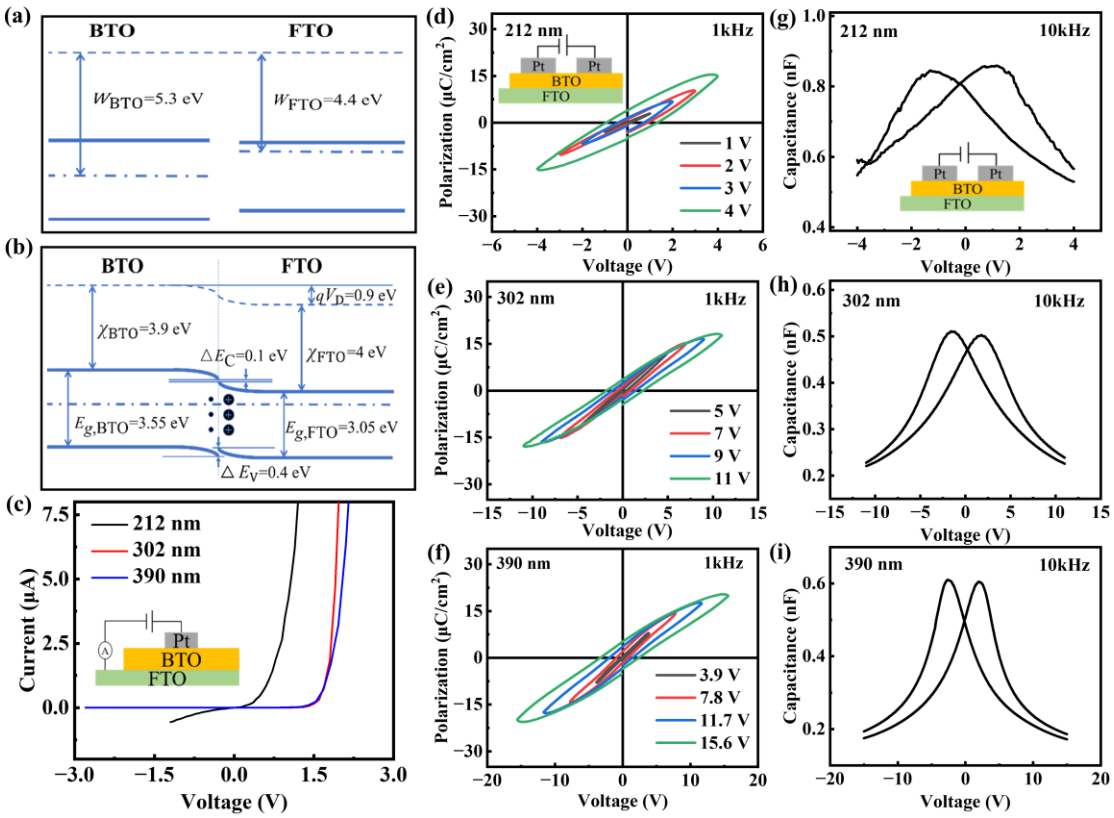


Figure 2. Equilibrium band diagrams of BTO and FTO (a) before and (b) after the formation of heterojunction. (c) *I-V* curves of the samples with different BTO thicknesses in dark. (d-f) *P-V* loops of the samples with different BTO thicknesses at 1 kHz under different applied voltages. (g-i) *C-V* loops of the samples with different BTO thicknesses at 10 kHz. The insets in (c, d, g) are the schematic diagram of the measurements.

Based on the above structural characterizations, the initial state of the samples can be anticipated.

There are two interfaces in the samples: Pt/BTO and BTO/FTO. As BTO is n-type conductive with a work function (5.30 eV) slightly lower than that of Pt (5.65 eV), there is a weak Schottky barrier at the Pt/BTO interface, which can be approximately regarded as ohmic contact. Therefore, the BTO/FTO interface plays the dominant role in the samples. Figure 2(a-b) present the band alignment diagrams of BTO and FTO before and after the formation of the heterojunction. When n-type FTO

with a smaller work function (4.4 eV) contacts with weak n-type BTO, electrons transfer from FTO (with a higher Fermi level) to BTO (with a lower Fermi level) until their Fermi levels align. Consequently, positively charged ionized donors accumulate on the FTO surface, while electrons gather on the BTO surface, forming an upward built-in electric field (pointing towards BTO), i.e., an n-n heterojunction. As mentioned above, with increasing BTO film thickness, $E_{VBM}^{E_f}$ gradually decreases and the Fermi level gradually lowers. The work functions of the BTO films with thicknesses of 212 nm, 302 nm, and 390 nm are 5.16 eV, 5.24 eV, and 5.30 eV, respectively. Correspondingly, the built-in potentials at the BTO/FTO heterointerface gradually increase, with values of 0.76 eV, 0.84 eV, and 0.90 eV, respectively, indicating a gradually increased interfacial barrier.

The existence of the interfacial barrier can be validated by the *I-V* characteristics. As shown in Figure 2(c), all the three Pt/BTO/FTO samples with different BTO thicknesses exhibit pronounced rectification behavior and forward conduction, with the 212 nm sample demonstrating the smallest turn-on voltage, corresponding to the lowest interfacial barrier. The upward built-in electric field at the BTO/FTO interface can promote the partial aggregation of oxygen vacancies near the BTO bottom surface. Meanwhile, it induces an initial upward (pointing from FTO to Pt) polarization in the as-grown BTO film, as verified by the Piezoresponse Force Microscopy (PFM) (Supplementary Figure S4). Furthermore, with the increase in the BTO thickness and the interfacial barrier height, the induced initial polarization in BTO may strengthen.

Considering the unidirectional conduction of the heterojunction, a two-top-electrode configuration was adopted for the macroscopic *P-V* loop measurement, where two Pt/BTO/FTO capacitors connected back-to-back.[26] As

shown in Figure 2(d-f), samples with different BTO thicknesses all exhibit pronounced ferroelectric hysteresis loops. The slightly rounded ends of the *P-V* loops at high voltages may be attributed to the carrier injection and migration across the BTO/FTO interface. Figure 2(g-i) illustrate that at 10 kHz, DC bias can significantly modulate the capacitance with hysteresis, which, accompanied by dielectric loss in normal range, further confirming the good ferroelectricity and the reversible polarization switching of the BTO (Figure S5).

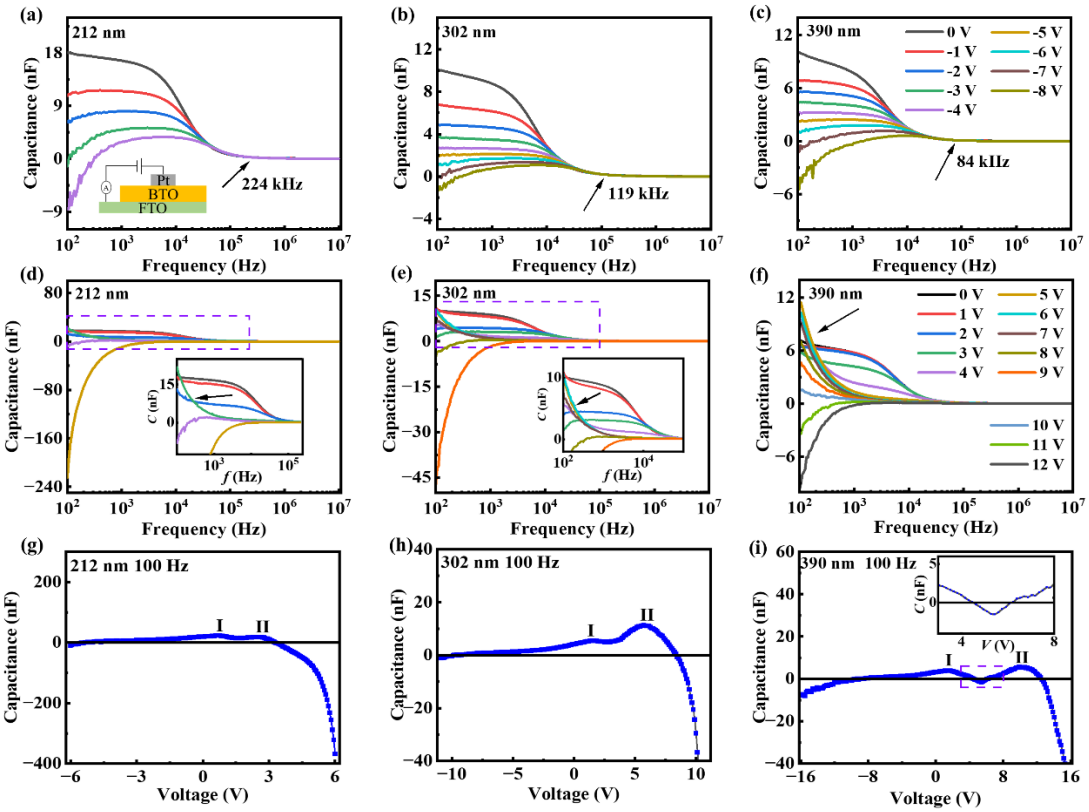


Figure 3. *C-f* curves under (a-c) negative and (d-f) positive bias, and (g-i) *C-V* curves at 100 Hz for the 212 nm, 302 nm, and 390 nm samples. Inset in (a) is the schematic diagram of the circuit, while the insets in (d, e, i) are the magnified images of the purple dashed box in each Figure. For the 390 nm sample, a negative total capacitance of approximately –1.53 nF emerges at a bias of 5.4 V, while the total capacitance under large biases of –16 V and +16 V are approximately –7.92 nF and –50.69 nF, respectively.

3.2 Capacitive Characteristics

Figure 3(a-f) present the *C-f* curves of the as-grown samples with different BTO thicknesses under negative and positive DC bias. At 0 V bias, all three samples exhibit polarization relaxation characteristics: with the increase of frequency from 100 Hz, the capacitance decreases slowly first, then drops rapidly around 10^3~10^4 Hz, and finally tends to stabilize at high frequencies above 10^5 Hz. This typical step-like variation in capacitance also indicates that the BTO is a ferroelectric with good insulating properties. Furthermore, at 0 V bias, the lower frequency limit for capacitance stabilization of the 212, 302, and 309 nm samples decreases gradually, being approximately 224 kHz, 119 kHz, and 84 kHz, respectively (indicated by black arrows in Figure 3(a-c)). This is consistent with the above anticipation on the initial polarization. The larger initial polarization in thicker samples possesses larger "inertia", and the dielectric activity of the dipoles in such samples is suppressed at lower frequencies.

Under negative and positive bias, generally, a significant decrease in capacitance at frequencies < 10^4 Hz is observed, while that at frequencies > 10^5 Hz hardly changes. At low frequencies, negative capacitance emerges under larger bias voltages. This phenomenon, observed here on BTO/FTO heterostructure with n-n junction, is similar to that reported earlier on BTO/p-Si heterostructure with p-n junction,[26] indicating that it is not limited to any specific heterojunction type.

An import new phenomenon is that, under moderate positive bias, all three samples exhibit an "abnormal" increase in low-frequency capacitance, as shown by the insets of Figure 3(d, e) and indicated by the black arrow in Figure 3(f).

Note that only some specific DC biases were applied during the measurement in Figure 3(a-f), to carefully analyze the influence of DC bias on negative capacitance, we selected a fixed frequency of 100 Hz, which favors the emergence of negative

capacitance, and measured the variation of sample capacitance by quasi-continuously increasing the voltage from the maximum negative bias to the maximum positive bias in 200 ascending steps. As shown in Figure 3(g-i), under negative bias, the capacitance monotonically decreases to negative values as the negative voltage increases. Under positive bias, two capacitance peaks (I and II) emerge sequentially with increasing voltage, followed by a sharp drop to negative values. These two capacitance peaks should correspond to the aforementioned "abnormal" increase in low-frequency capacitance. More interestingly, the 390 nm sample also exhibits a negative capacitance region under small bias, around the valley between the two capacitance peaks, as shown in the inset of Figure 3(i). As a comparison, no negative capacitance was observed in the BTO/Pt control sample we prepared.

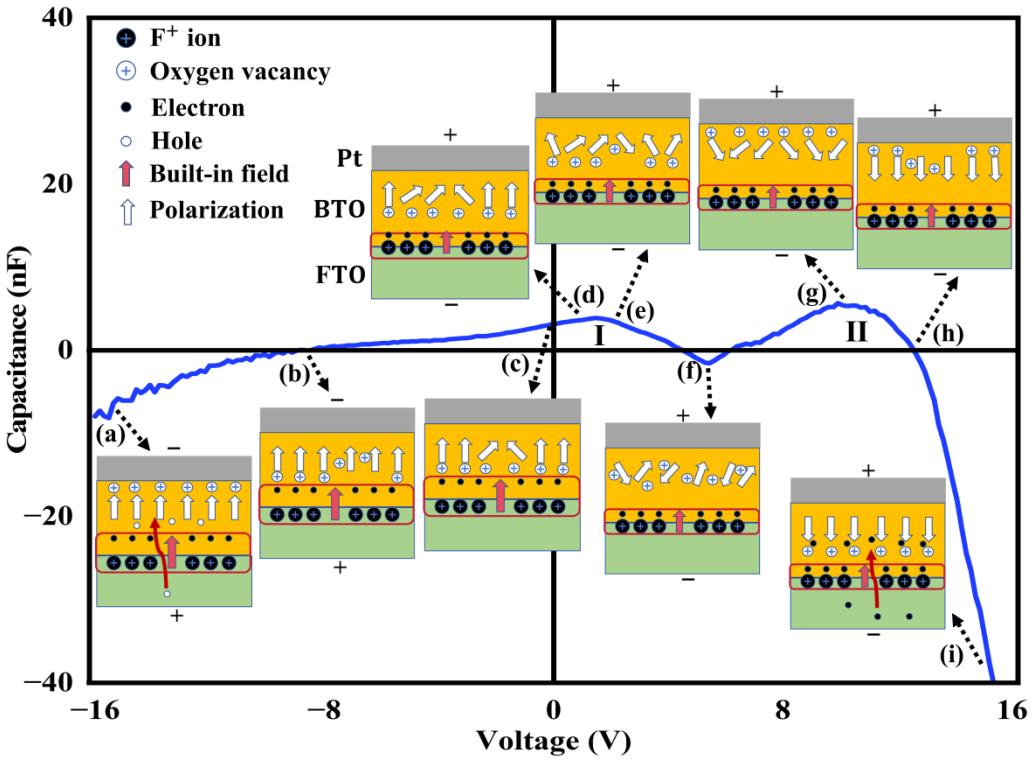


Figure 4. Polarization switching and charge transfer of the sample under different bias.

3.3 Mechanisms of Capacitance Evolution

When a step voltage ΔV is applied, the total capacitance C of the sample can be

given by equation (1).

$$C(\omega)=C_0+\frac{1}{\omega\Delta V}\int_0^{\infty}\left[-\frac{d\delta j(t)}{dt}\right]\sin\omega t\,dt=C_0+C_a \quad (1)$$

Where C_0 represents positive geometric capacitance, dominated by the dipoles (polarization). C_a is the additional capacitance due to relaxation current ($\delta j(t)$) from lagged charge migration (including oxygen vacancies and carriers).[28,34] If $\delta j(t)$ increases over time (t), C_a and even the total capacitance (C) can be negative.[37,38] In this case, equation (1) can be simply expressed as:

$$C = C_0 - |\,C_a\,| \quad (2)$$

It is noteworthy that both the polarization response and the lagged migration of charge carriers, as two representative dielectric relaxation processes, exhibit significantly enhanced activity in the low-frequency regime.[28,39] In the following, we would interpret the two negative capacitance behaviors observed for the Pt/BTO/FTO structure at low frequencies, on the basis of equation (2) (Figure 4). For clarity, we denote the negative capacitance under large bias and that under small bias as NCl and NCs, respectively, and the evolution of capacitance is elucidated in a stepwise manner across the entire bias sweep sequence, which spans from the maximum negative bias to the maximum positive bias.

(1) Under a negative bias from bottom to top, the heterojunction is reverse-biased, the interface barrier is enhanced, and the AC testing voltage division across the BTO layer decreases, leading to a suppressed total capacitance.

At maximum negative bias, the electric dipoles are maximally oriented upward, corresponding to low dielectric activity and a small C_0. Meanwhile, although a large number of oxygen vacancies in BTO are electrostatically driven toward the top interface by the applied negative bias, with suppressed dielectric activity, the minority carriers (holes) in FTO are driven across the interfacial barrier into BTO to

compensate for the polarization charges. Their lagged motion under the AC testing voltage dominates the relaxation current, leading to a large $|C_a|$, which in turn gives rise to a negative total capacitance *C* (NCl, inset a in Figure 4). For the 390 nm BTO film, the total capacitance is approximately -7.92 nF (100 Hz) under a bias of -16 V.

At moderate negative bias, although the dipoles still point upward, the dielectric activity is significantly enhanced and C_0 increases. Meanwhile, the minority carriers (holes) in FTO return, and the oxygen vacancies at the upper interface migrate toward the bottom interface driven by the depolarization field of BTO, contributing a relatively small relaxation current and additional capacitance $|\square_{\square}|$ under the AC testing electric field. The total capacitance *C* transitions from negative to positive values (inset b in Figure 4).

As the negative bias approaches zero, a small portion of dipoles may deviate from the direction of the external electric field, and the geometric capacitance C_0 of the sample continues to increase. Meanwhile, as a large number of oxygen vacancies in BTO are confined at the bottom interface as screening charges, their dielectric activity is suppressed, and the relaxation current and $|C_a|$ also decreases, resulting in a gradual increase in the positive total capacitance *C* (inset c in Figure 4).

(2) Under a positive bias from top to bottom, the heterojunction is forward-biased, the interface barrier is lowered, and the AC testing voltage division across the BTO layer increases, leading to an enhanced total capacitance.

As the positive bias slightly increases from zero, more dipoles deviate from the vertical upward direction, the dipole activity continues to strengthen, and C_0 increase monotonically. At this moment, a large number of oxygen vacancies in BTO still reside at the bottom interface, the relaxation current and $|C_a|$ are maintained at a relatively low level, and the total capacitance *C* exhibits a gradual increasing trend

(inset d in Figure 4).

When the positive bias exceeds V_e, the dipoles in the BTO layer begin to switch from the upward to the downward direction, and the polarization intensity, together with C_0, decreases accordingly. Concurrently, the oxygen vacancies that were originally confined at the bottom interface of BTO as screening charges are gradually released into the BTO interior, the relaxation current and the additional capacitance $|C_a|$ increase slightly, and the total capacitance C gradually decreases, forming peak I (inset e in Figure 4)

When the positive bias reaches V_f, nearly half of the dipoles have completed switching, the polarization intensity of BTO is nearly zero, and C_0 reaches its minimum value. At this time, the number of oxygen vacancies inside BTO reaches its maximum value, and the relaxation current and $|C_a|$ contributed under the alternating electric field also reach their maximum values, so the total capacitance C exhibits a minimum value (inset f in Figure 4).

When the positive bias exceeds V_f, the dipoles in BTO continue to switch downward, and the polarization intensity of the sample increases from zero, so does C_0. Simultaneously, oxygen vacancies are electrostatically driven toward the upper interface as screening charges, the number of oxygen vacancies in the BTO bulk that contribute to the relaxation current decreases, and $|\square_{\square}|$ decreases accordingly. Consequently, the total capacitance C increases. When the bias increases to V_g, nearly all dipoles in BTO have turned downward, and a large number of oxygen vacancies are confined at the upper interface, giving rise to total capacitance peak II (inset g in Figure 4).

As the positive bias continues to increase, the ordering degree of dipoles aligned downward along the external field increases while the dielectric activity decreases,

and C_0 begins to decrease. Meanwhile, the oxygen vacancies at the upper interface are driven by the larger external field to migrate toward the BTO interior and even to the bottom interface. The oxygen vacancies remaining inside BTO contribute to the relaxation current and the increased $|C_a|$, and the total capacitance begins to decrease again. When the bias increases to V_h, the total capacitance C transitions from positive to negative values (inset h in Figure 4).

At maximum positive bias, the dielectric activity of dipoles aligned along the external electric field is strongly suppressed, and C_0 decreases significantly. At this time, although a large number of oxygen vacancies are driven by the external field to the vicinity of the BTO bottom interface, with their dielectric activity suppressed, the majority carriers (electrons) in FTO are driven across the barrier into BTO to compensate for the polarization charges. Their lagged migration under the AC testing electric field generates a large |□□|, causing C to drop sharply (NCl, inset i in Figure 4). For the 390 nm BTO film, the total capacitance is approximately -50.69 nF (100 Hz) under a bias of 16 V.

The above discussions reveal that the two capacitance peaks (Peak I and Peak II) that appear during the gradual increase of positive bias correspond to the onset and termination of dipole switching, respectively. For the 390 nm sample between capacitance peaks I and II, on the one hand, during dipole switching, the sample passes through a zero-polarization state, corresponding to a small C_0. On the other hand, as discussed above, a stronger initial polarization is induced in the thicker BTO film. Accordingly, during the intermediate stage of dipole switching, a larger number of oxygen vacancies, acting as screening charges, migrate from the interface into the BTO bulk, resulting in a larger relaxation current and an additional capacitance |□□| under the AC testing electric field. If the additional capacitance of the 212 nm

sample is denoted as $|\square_{\square I}|$, that of the 390 nm sample can be expressed as $|\square\square_{\square I}|(n > 1)$. The above two factors lead to the presence of a negative total capacitance even under a relatively small bias (NCs). For the 390 nm sample, the total capacitance is approximately −1.53 nF (100 Hz) under a samller bias of 5.4 V. Notably, between peak I and peak II, which precisely corresponds to the intermediate regime of polarization switching where the intrinsic negative capacitance effect theoretically emerges in ferroelectric materials,[2] we experimentally observed a negative total capacitance value for the first time.

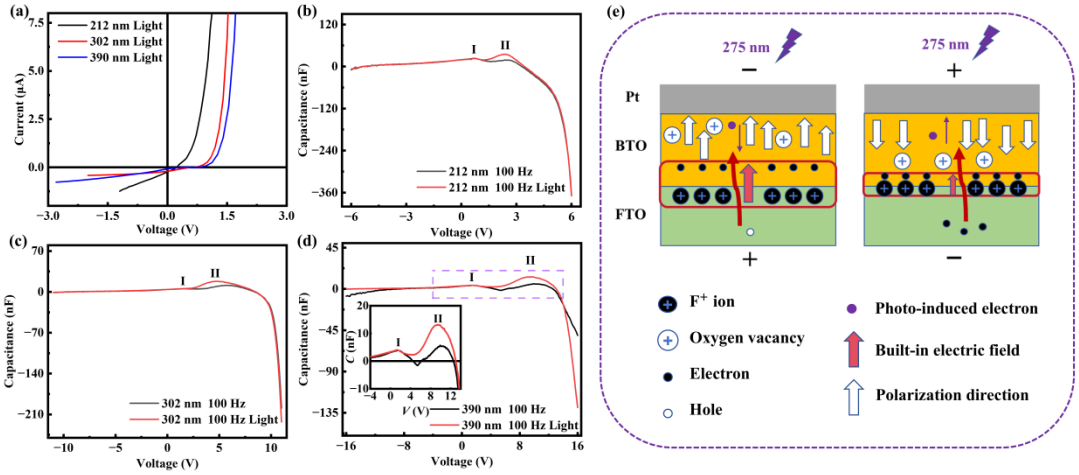


Figure 5. (a) *I-V* curves of samples with different BTO thicknesses under 275 nm ultraviolet light. Influence of ultraviolet light on the *C-V* curves for the (b) 212 nm, (c) 302 nm, and (d) 390 nm sample. (e) Schematic diagram of the UV light impact on the charge migration in the samples under large negative and positive bias. Under UV illumination, the total capacitance of the 390 nm sample at 5.4 V bias increases from –1.53 nF to 2.92 nF; while at large bias magnitude of –16 V and +16 V, the total capacitance values evolve to approximately –0.23 nF and –129.29 nF, respectively.

3.4 UV light Modulation of Capacitance

Light illumination can regulate the electrical properties of the Pt/BTO/FTO structure. To demonstrate this, the sample surface was illuminated with 275 nm

ultraviolet (UV) light, which has an energy higher than the absorption edge of BTO. Unlike in dark (Figure 2(c)), all the three samples exhibit pronounced current at zero bias under UV illumination (Figure 5(a)), and the photocurrents are negative. This indicates that the BTO film can absorb UV light, and the photocarriers can be efficiently separated and directed by the built-in electric field at the BTO/FTO interface.

Figure S6 and Figure 5(b-d) show the impact of UV light illumination on the *C-f* and *C-V* curves of the samples. Three phenomena need to be noticed and explained.

1. Under large negative or positive bias, UV light oppositely influences NCl due to different dominant charge carriers. At large negative bias (Figure 5(e)), the minority carrier (hole) migration from FTO to BTO dominates. Under UV light, the photoelectrons in BTO move towards FTO and easily recombine with holes, reducing the hole concentration in FTO, and leading to smaller relaxation current and NC (absolute) value. For the 390 nm BTO film, under a bias of -16 V, the total capacitance changes from approximately -7.92 nF to -0.23 nF (100 Hz). Conversely, at large positive bias, the majority carrier (electron) migration from FTO to BTO dominates. Under UV light, photoelectrons in BTO move towards the Pt electrode (Figure 5(e)), in the same direction as the majority carriers, increasing the relaxation current and the NCl (absolute) value. For the 390 nm BTO film, under a bias of 16 V, the total capacitance changes from approximately -50.69 nF to -129.29 nF (100 Hz).

2. Under positive bias, the capacitance peak II becomes more pronounced and shifts to smaller bias. The directional movement of photocarriers accelerates the polarization switching in BTO, allowing it to accomplish at smaller bias. Meanwhile, photogenerated carriers can partially screen the polarization charges, reduce the migration of oxygen vacancies accompanying the aforementioned polarization

switching, and correspondingly decrease the relaxation current and | □□ | which increases the total capacitance near peak II and eliminate the NCs region between peaks I and II in the 390 nm sample.

3. The impact of UV illumination is more pronounced in thicker samples. As mentioned above, the influence of UV light mainly manifests in the directional movement of photocarriers under external bias. Under steady-state illumination, the effective photocarrier concentration can be expressed as [40-42]:

$$\Delta n \propto \frac{KP}{N_t d} \qquad (2)$$

where K is a parameter that incorporates the effects of the carrier-generation quantum efficiency η, reflectivity R, photon energy $h\upsilon$, absorption coefficient α, defect capture cross-section σ, and carrier thermal velocity V_{th}, while P, d, and N_t denote the incident light power density, the effective light-absorbing layer thickness, and the defect concentration, respectively. Considering that the absorption coefficient of BTO in the deep-ultraviolet region has been reported to reach the order of $10^5 cm^{-1}$ [43,44], if the depth at which the light intensity decays to $\frac{1}{e}$ of its initial value is taken as the effective light-absorbing layer thickness d, d for 275 nm light in BTO is approximately 100 nm, which is much smaller than the BTO layer thicknesses in our samples. In other words, for all the samples with BTO thicknesses of 212, 302, and 390 nm, the 275 nm ultraviolet light is strongly absorbed within an effective near-surface absorbing layer of approximately 100 nm. Then, it can be seen from Equation (2) that, for a constant d, the effective photocarrier concentration in the absorbing surface layer of the three samples is positively correlated with the incident

light power density and inversely correlated with the defect concentration. In this case, on the one hand, our samples contain noticeable oxygen vacancy defects that can readily trap the small amount of photocarriers generated under weak illumination, making the changes in the negative capacitance visible only under relatively strong ultraviolet illumination with a power density of 5600 $\mu W/cm^2$. On the other hand, the thicker 390 nm sample contains a lower concentration of oxygen vacancy defects, which enables a higher effective photocarrier concentration and thus a more pronounced modulation of negative capacitance.

It should be noted that, 275 nm ultraviolet light was selected in this work for two main reasons: band alignment and experimental comparability. On the one hand, the photon energy of 275 nm light is approximately 4.51 eV, which is significantly higher than the BTO band gap (3.55 eV). Therefore, 275 nm illumination can effectively induce interband transitions and generate sufficient electron-hole pairs within the films, thereby modulating the negative capacitance behavior under different bias. On the other hand, as discussed above, the penetration depth (effective light-absorbing thickness) of 275 nm ultraviolet light is similar in the BTO films with thicknesses of 212, 302, and 390 nm. This facilitates comparison of the experimental results from the three samples and helps obtain a reliable and reasonable understanding of the underlying mechanism.

3.4 Discussion on Underlying Mechanisms and Potential Applications

Building upon the experimental observations of the two distinct types of negative capacitance, we further discuss their underlying mechanisms and potential applications.

The negative capacitance detected at small bias (NCs) corresponds to the intermediate state of polarization switching. If a highly conductive metal electrode is used, the ferroelectric polarization charge can be screened instantly, and the system would leap over the metastable state and reach thermodynamic equilibrium almost immediately. As a result, the fleeting intrinsic NC signature is masked. In a ferroelectric-insulator series stack, the insulating dielectric layer blocks the screening charges, suppresses ferroelectric polarization switching, and yields a distinct voltage window where the total capacitance exceeds the bare dielectric layer capacitance,[13,14] which corresponds to the regime where intrinsic negative capacitance effect emerges. Considering that polarization switching and charge carrier migration are two typical relaxation processes in ferroelectric oxides -- both of which exhibit high sensitivity to external conditions such as electric fields and interfaces -- in this work, the BTO film was deposited on a semiconducting FTO substrate. On one hand, the stepwise DC bias sweep effectively retards the polarization-switching dynamics. On the other hand, the relaxation migration of oxygen vacancies, which are readily trapped at the interface, significantly slows down the screening charge compensation process. This dual-delay effect provides a critical time window for capturing the metastable process of ferroelectric polarization switching, and is also responsible for the minimum in the *C-V* curve under small bias for all the samples with different thicknesses. The thicker 390 nm sample possesses a larger initial polarization, and the dipole switching of which is correlated with the migration of a larger number of oxygen vacancies (as screening charges), corresponding to a larger relaxation current/negative additional capacitance, enabling the emergence of a negative total capacitance (5.4 V bias, −1.53 nF, 100 Hz). In this work, a negative total capacitance is directly measured within the voltage range corresponding to the intermediate state of polarization switching, which

can provide a material and structural reference for the design of low-power NCFET devices.

The negative capacitance observed under large bias (NCl) primarily originates from carrier injection across the interfacial barrier and their subsequent lagged migration, following the completion of polarization switching. The relaxation current accompanying the NCl can be utilized to emulate biological synaptic behavior , potential for applications in the field of neuromorphic computing.

Furthermore, we elucidate the underlying physical mechanism for modulating the negative capacitance effect via UV induced non-equilibrium carriers. This finding not only provides a novel pathway for multi-degree-of-freedom control of reconfigurable synaptic devices, but also expands the application scope of ferroelectric/semiconductor heterojunctions in in-sensor computing systems.

4. Conclusion

We prepared ferroelectric $BaTiO_3$ films on FTO substrates using pulsed laser deposition, the Pt/BTO/FTO heterostructure exhibits two distinct negative capacitance (NC) under DC bias. One occurs at small positive bias, corresponding to the intermediate state of ferroelectric polarization switching, and attributed to the delayed polarization switching and oxygen vacancy migration. The other occurs at large positive and negative bias, originating from carrier migration across the interfacial barrier. UV illumination increases the carrier density in BTO, which effectively regulate the NC values through synergistically adjust the polarization switching and charge migration. The two types of negative capacitance, possessing distinct physical mechanisms, are applicable in different fields: the former can provide core support for the construction of ultra-low-power negative-capacitance field-effect transistors,

while the latter is suitable for simulating artificial biological synaptic behavior. Furthermore, UV illumination offers a non-invasive route to tune the performance of NC-based devices. It should be noted that the present study only focuses on BTO thin films with three distinct thicknesses deposited on conventional FTO substratess, along with a single fixed wavelength and light intensity for UV illumination. The analysis of the negative capacitance effect and its underlying regulation mechanism remain at the qualitative level. From the experimental perspective, subsequent work will expand the scope of explored material systems, carry out more systematic and in-depth investigations on the light modulation phenomena, and precisely regulate the carrier concentration of FTO substrates via microfabrication processes, so as to explore the fabrication routes for high-performance NCFET devices. From the theoretical perspective, the Landau-Ginzburg-Devonshire model and Poisson-Schottky equation will be introduced for co-simulation, to further deepen the understanding of the physical essence of the negative capacitance effect and realize the quantitative control of the negative capacitance value. On this basis, a more adaptable theoretical model will be established to quantitatively predict the subthreshold swing limit of the corresponding NCFET and the weight modulation interval of artificial synapse, providing key experimental support and theoretical reference for the future development of low-power logic, neural morphology computing, and optoelectronic integrated systems based on ferroelectric/semiconductor heterojunctions.

Acknowledgments

This work was supported by the Ministry of Science and Technology of the People´s Republic of China (Nos. 2025YFF0520301, and 2022YFA1402903), the

National Natural Science Foundation of China (Nos. 52172116, 12574097, and 12204246), and the Priority Academic Program Development of Jiangsu Higher Education Institutions (PAPD).

References

[1] Khan A I, Chatterjee K, Wang B, Drapcho S, You L, Serrao C, Bakaul S R, Ramesh R and Salahuddin S 2015 *Nat. Mater.* **14** 182

[2] Íñiguez J, Zubko P, Luk'yanchuk I and Cano A 2019 *Nat. Rev. Mater.* **4** 243

[3] Hoffmann M, Fengler F P G, Herzig M, Mittmann T, Max B, Schroeder U, Negrea R, Pintilie L, Slesazeck S and Mikolajick T 2019 *Nature* **565** 464

[4] Qin Y and Li J 2024 *Phys. Rev. B* **110** 134101

[5] Pradhan J R and Dasgupta S 2024 *ACS Appl. Mater. Interfaces* **16** 39517

[6] Liu J, Han W, Hong E, Deng M, Li Z, Wu L and Fang X 2025 *Adv. Funct. Mater.* **35** 2425350

[7] Min J H, Jang S C, Kim K J, Rim Y S and Kim H S 2025 *Mater. Today Electron.* **14** 100178

[8] Xu J, Jiang S Y, Zhang M, Zhu H, Chen L, Sun Q Q and Zhang D W 2018 *Appl. Phys. Lett.* **112** 103104

[9] Zhao L, Liang Y, Ma J, Pan Z, Liu X, Yang M, Sun Y, Gao W, Li B, Li J and Huo N 2023 *Adv. Funct. Mater.* **33** 2306708

[10] Kamaei S, Liu X, Saeidi A, Wei Y, Gastaldi C, Brugger J and Ionescu A M 2023 *Nat. Electron.* **6** 658

[11] Chi M, Li A, Zhang X, Li Z, Jia M, Wang J, Wang Z L and Zhai J 2024 *Nano Energy* **126** 109640

[12] Saha A K and Gupta S K 2021 *J. Appl. Phys.* **129** 080901

[13] Park H W, Byun S, Kim K D, Ryoo S K, Lee I S, Lee Y B, Lee S H, Nam H W, Lee J H, Song J H, Shin S J and Hwang C S 2023 *Adv. Funct. Mater.* **33** 2304754

[14] Wu Y, Yang H, He Q, Huang J, Chen W, Tan C, Zhang Y and Zheng Y 2025 *ACS Nano* **19** 21997

[15] Ansari E, Martinolli N, Hartmann E, Varini A, Stolichnov I and Ionescu A M 2025 *Nano Lett.* **25** 2702

[16] Chen Q, Wu Y, He J, Tan C, Zhang H, Zhong X, Chen J, Song H, Li J, Wang J and Zhong G 2025 *J. Appl. Phys.* **138** 074106

[17] Chang S C, Avci U E, Nikonov D E, Manipatruni S and Young I A 2018 *Phys. Rev. Appl.* **9** 014010

[18] Park H W, Oh M and Hwang C S 2022 *Adv. Funct. Mater.* **32** 2200389

[19] Boni A G, Chirila C F, Filip L D, Botea M I, Radu C, Popescu D G, Husanu M A, Hrib L, Trupina L, Pintilie I and Pintilie L 2025 *Acta Mater.* **298** 121177

[20] Tasneem N, Ravindran P V, Wang Z, Gomez J, Hur J, Yu S, Datta S and Khan A I 2021 *Appl. Phys. Lett.* **118** 122901

[21] Qiao L, Zhao R, Song C, Zhou Y, Wang Q, Ren T L and Pan F 2024 *Mater. Futures* **3** 011001

[22] Qin Y and Li J 2024 *Phys. Rev. B* **110** 134101

[23] Yuan G, Lei Y, Dong Y, Li C and Li J 2026 *Appl. Phys. Lett.* **128** 142903

[24] Daw D, Bouzid H, Jung M, Suh D, Biswas C and Lee Y H 2024 *Adv. Mater.* **36** 2304338

[25] Hou Y F, Li W L, Zhang T D, Yu Y, Han R L and Fei W D 2016 *ACS Appl. Mater. Interfaces* **8** 22354

[26] Wang Z, Li H, Hu H, Fan Y, Fan R, Li B, Zhang J, Liu H, Fan J, Hou H, Dang F, Kou Z and Guo Z 2020 *Adv. Electron. Mater.* **6** 1901005

[27] Acharya J, Goul R, Wilt J and Wu J 2020 *ACS Appl. Mater. Interfaces* **12** 9902

[28] Liu L, Lei L, Lu X, Xia Y, Wu Z and Huang F 2023 *ACS Appl. Mater. Interfaces* **15** 10175

[29] Mazet L, Yang S M, Kalinin S V, Schamm-Chardon S and Dubourdieu C 2015

584 *Sci. Technol. Adv. Mater.* **16** 036005
585 [30] Yu P, Wang W, Zheng T, Wan X and Jiang Y 2023 *ACS Appl. Mater. Interfaces* **15**
586 46031
587 [31] Karvounis A, Timpu F, Vogler-Neuling V V, Savo R and Grange R 2020 *Adv.*
588 *Optical Mater.* **8** 2001249
589 [32] Nassar M H and El-Nowihy G H 2025 *ACS Appl. Energy Mater.* **8** 16066
590 [33] Kananke Udubokke Rathnayakage R S R, Bandara T M W J, Wijayaratne K,
591 Kumara G R A, de Silva L A and Tennakone K 2023 *ACS Appl. Energy Mater.* **6** 8336
592 [34] Ershov M, Liu H C, Li L, Buchanan M, Wasilewski Z R and Jonscher A K 1998
593 *IEEE Trans. Electron Devices* **45** 2196
594 [35] Yang Y, Wang X, Sun C and Li L 2009 *Nanotechnology* **20** 055709
595 [36] Pan R, He Y, Li M, Li P, Liu P and Xia Z 2014 *Mater. Sci. Eng. B* **188** 84
596 [37] El Kamel F, Gonon P, Jomni F and Yangui B 2008 *Appl. Phys. Lett.* **93** 042904
597 [38] Ke Q, Lou X, Yang H, Kumar A, Zeng K and Wang J 2012 *Appl. Phys. Lett.* **101**
598 022904
599 [39] Gupta P, Mahapatra P K and Choudhary R N P 2020 *phys. status solidi B* **257**
600 1900236
601 [40] Oshina I and Spigulis J 2021 *J. Biomed. Opt.* **26** 100901
602 [41] Shockley W and Read W T Jr 1952 *Phys. Rev.* **87** 835
603 [42] Suproniuk M, Wierzbowski M and Paziewski P 2020 *Sci. Rep.* **10** 11865
604 [43] Maes J, Balcaen L, Drijvers E, Zhao Q, De Roo J, Vantomme A, Vanhaecke F,
605 Geiregat P and Hens Z 2018 *J. Phys. Chem. Lett.* **9** 3093
606 [44] Green M A and Keevers M J 1995 *Prog. Photovolt.: Res. Appl.* **3** 189